
Ionization Dynamics of Molecules in Intense Laser Fields

Thomas Kim Kjeldsen

Department of Physics and Astronomy
University of Århus

Progress report
May 2005

Contents

Preface	ii
Acknowledgements	ii
1 Introduction	1
2 Ionization theory	2
2.1 Molecular strong-field approximation	2
2.1.1 Qualitative discussion of the effect of nuclear motion	6
2.2 Molecular tunneling theory	6
2.3 Ion signal	9
2.4 Results	11
2.4.1 Orientational dependent ionization	11
2.4.2 Diatomic molecules and companion atoms	13
2.4.3 Vibrational distributions	15
3 Exact one-electron solution	19
3.1 The split step method	19
3.2 Propagation in the spherical harmonics basis	21
3.2.1 H_2^+ in a time dependent linearly polarized electric field	22
3.2.2 Benchmark: spherical harmonics- versus space representation	25
3.2.3 Extension to multielectron molecules	26
3.3 Ionization probability	27
4 Outlook	29

Preface

This progress report contains a summary of my work made in the part A of my Ph.D. studies at the Department of Physics and Astronomy, University of Aarhus.

The main part of the report is divided in two separate chapters. Most of the work during the two year period concerns the theory outlined in chapter 2. This work has resulted in four published papers [1–4] and one paper is submitted for publication at the time of writing [5].

Towards the end of part A, I have studied a different theory which is described in the second part of the report in chapter 3. Work on this part is still in progress and no results will be presented.

Unless otherwise stated, atomic units [$m_e = |e| = \hbar = 1$] will be used throughout this report.

Acknowledgements

First of all I would like to thank my project supervisor Lars Bojer Madsen for excellent supervision throughout the last couple of years. My experimental collaborators in Århus, Henrik Stapelfeldt and Christer Z. Bisgaard and my theoretical collaborators in Bergen, Jan-Petter Hansen, Morten Førre and Sølve Selstø also deserve a great thank for many useful discussions along the way. Finally, I would like to thank Anders S. Mouritzen for proofreading this manuscript.

Thomas Kjeldsen, May 2005

1. Introduction

When an atom or a molecule is exposed to an intense laser field a series of non-perturbative phenomena may occur. In the present context an intense laser field is characterized by a field strength which is comparable to the Coulomb interaction between the electrons and the nuclei. The typical intensities for this to be the case are $10^{13} - 10^{15} \text{ Wcm}^{-2}$. With the development of mode locking laser techniques, especially from the eighties and onwards, these high intensities are now readily available from commercial laser systems. Typically such lasers will emit short pulses with a duration of less than 100 fs at an infrared central wavelength. This laser light will interact non-resonantly with the electrons of the atomic or molecular system. In the early days of strong-field physics, the experimental and theoretical studies were primarily concentrated on atoms. In spite of theoretical advances in modelling of atoms in laser fields, it is still too difficult to carry out a full *ab initio* calculation of a multi-electron atom and, hence, the theoretical understanding must rely on some kind of approximation and theoretical modelling.

A simple qualitative understanding of the dynamics may be obtained with the so-called rescattering model [6], which accounts well for many observed phenomena. The rescattering model is divided in several steps. In the first step, the atom is ionized by the field to produce an electron in the continuum and a residual ion. The electron is influenced by the oscillating laser field which can drive the electron back to the parent ion where a rescattering event can occur. Several different effects have been observed experimentally, depending on the type of scattering, e.g., an inelastic scattering excites the residual ion and will lead to an enhancement in the yield of doubly charged ions. If, on the other hand, the electron recombines with the ion, the excess energy will be ejected in one photon with a frequency being a multiple of the laser frequency. This phenomenon is known as high order harmonic generation and is by now routinely used to produce coherent XUV pulses.

Single ionization is thus the initial key process and a detailed understanding of this step is critical for the further understanding of rescattering dynamics. While ionization of atoms has been extensively studied the equivalent studies on molecules are less developed. Molecules are much more complex to model theoretically than atoms as they contain additional nuclear degrees of freedom and, consequently, nuclear rotational and vibrational dynamics must be taken into consideration. Ionization of atoms has been modelled very successfully by one-electron models with two of the most widely used models being the quasistatic tunneling theory and the strong-field approximation. In chapter 2 of this report these models are generalized to cover molecules and several results obtained with these models are presented. A more computationally demanding method, which solves the one-electron dynamics exactly, is discussed in chapter 3. In chapter 4 an outlook for the future plans is given.

2. Ionization theory

In this chapter we describe the generalization of the atomic strong-field approximation (SFA) [7–9] to cover molecules. This generalized model is called the molecular strong-field approximation (MO-SFA). We will also discuss a similar generalization of the atomic Ammosov-Delone-Krainov (ADK) [10] tunneling theory to give the molecular tunneling (MO-ADK) theory. Both theories will be developed within the single active electron approximation, i.e., only the most loosely bound electron is assumed to couple significantly to the field.

The results presented in this chapter only cover diatomic molecules. However, the theories can equally well be applied to polyatomic molecules as we have demonstrated in Refs. [1, 3].

2.1 Molecular strong-field approximation

In the strong-field approximation we seek a transition amplitude corresponding to the transition between approximate initial and final states induced by an electromagnetic field. The field is assumed to be periodic with constant amplitude and is turned on adiabatically.

Using the Coulomb gauge and the dipole approximation, the linearly polarized laser field may be described by the vector potential $\mathbf{A}(t) = \mathbf{A}_0 \cos \omega t$, where ω is the angular frequency. The scalar potential vanishes in the Coulomb gauge since it is determined only from the charge distribution which is zero everywhere. Any spatial variation of the field is neglected in the dipole approximation. The electric field is obtained as $\mathbf{F}(t) = -\partial_t \mathbf{A}(t)$, i.e., $\mathbf{F}(t) = \mathbf{F}_0 \sin \omega t$, and the intensity is $I = F_0^2$. The interaction between the field and an N -electron system in the velocity gauge is

$$V_N^{(\text{VG})}(t) = \sum_{j=1}^N \mathbf{A}(t) \cdot \mathbf{p}_j + \frac{\mathbf{A}^2(t)}{2}, \quad (2.1)$$

and in the length gauge

$$V_N^{(\text{LG})}(t) = \sum_{j=1}^N \mathbf{r}_j \cdot \mathbf{F}(t). \quad (2.2)$$

The velocity gauge representation is obtained by a minimal coupling of the electrons to the electromagnetic field, $\mathbf{p}_j \rightarrow \mathbf{p}_j + \mathbf{A}(t)$ and the length gauge representation is connected to the velocity gauge representation by a unitary transformation, see e.g. Ref. [11]. In any exact theory, observables are invariant under unitary transformations. In approximate theories, including the SFA, this invariance may not be preserved. Here we will derive an expression for the ionization rate in both gauges, and we shall return to the discussion of choice of gauge in Sec. 2.4. In either gauge, we express the angular

differential rate $dW/d\hat{q}$ and total rate W as sums over n -photon absorptions [12]

$$\frac{dW}{d\hat{q}} = 2\pi \sum_{n=n_0}^{\infty} |A_{qn}|^2 q_n, \quad (2.3)$$

$$W = 2\pi \sum_{n=n_0}^{\infty} \int |A_{qn}|^2 q_n d\hat{q}, \quad (2.4)$$

where the transition amplitudes corresponding to the interaction $V_N^{(c)}(t)$, ($c = \{\text{VG, LG}\}$),

$$A_{qn}^{(c)} = \frac{1}{T} \int_0^T \langle \Psi_f | V_N^{(c)}(t) | \Psi_i \rangle dt, \quad (2.5)$$

involves integration over one period of the field $T = \frac{2\pi}{\omega}$, and $\langle || \rangle$ designates integration over both the electronic *and* nuclear coordinates. Here Ψ_i is the molecular initial state and Ψ_f is the final state describing the state of the residual ion and the free electron in the laser field. In Eqs. (2.3)-(2.4), n_0 is the minimum number of photons needed to reach the continuum, and the momentum q_n is given by energy conservation. In the Born-Oppenheimer approximation q_n is determined by Eq. (2.12) below.

In the SFA we approximate the initial state by a field-free molecular state. In the Born-Oppenheimer approximation this state is a product of an electronic state and a vibrational state labelled by a number of vibrational quantum numbers ν_i corresponding to each normal mode. Here we will consider a diatomic molecule with just one vibrational mode, but the theory can easily be extended to cover polyatomic molecules. The initial electronic and vibrational states are typically the respective ground states. The rotational periods of molecules are much longer than typical experimental pulse durations and therefore the rotational degrees of freedom may be neglected. The total energy of the initial state is

$$E_i = E_i^e(R_0) + E_{\nu_i}, \quad (2.6)$$

where $E_i^e(R_0)$ is the electronic eigenenergy at the internuclear equilibrium distance R_0 and E_{ν_i} is the vibrational eigenenergy of the nuclear Hamiltonian. If we approximate the electronic part of the initial wave function by the single-determinant Hartree-Fock wave function, the corresponding initial molecular wave function is

$$\Psi_i = \frac{1}{\sqrt{N!}} \det | \psi_1(\mathbf{r}_1) \psi_2(\mathbf{r}_2) \dots \psi_N(\mathbf{r}_N) |_{R_0} \chi_{\nu_i}(R) e^{-iE_i t},$$

where $\chi_{\nu_i}(R)$ is the initial vibrational wave function and the ψ_j 's are orthogonal single-electron wave functions. The electronic wave function is evaluated at the nuclear equilibrium distance R_0 since we assume, consistent with the Born-Oppenheimer picture, that it will be a slowly varying function of the internuclear distance.

In order to describe the process of single ionization, we seek the transition amplitude to a single-electron continuum state and a definite vibrational and electronic eigenstate of the molecular ion. The main approximation in the SFA is to assume that the

continuum electron couples much more strongly to the field than to the residual ion. In this way, the ion-electron interaction can be neglected in the final state. The continuum wave function should then satisfy

$$i\partial_t\psi_V^{(c)}(\mathbf{r},t) = \left(p^2/2 + V^{(c)}(t)\right)\psi_V^{(c)}(\mathbf{r},t), \quad (2.7)$$

where $V^{(c)}(t)$ is the single term of the interaction operators, Eqs (2.1) and (2.2), which acts on the continuum electron. By direct substitution, we may easily verify that wave functions of the form

$$\psi_V^{(\text{LG})}(\mathbf{r},t) = (2\pi)^{-3/2} \exp \left[i(\mathbf{q} + \mathbf{A}(t)) \cdot \mathbf{r} - \frac{i}{2} \int_{-\infty}^t (\mathbf{q} + \mathbf{A}(t'))^2 dt' \right] \quad (2.8)$$

$$\psi_V^{(\text{VG})}(\mathbf{r},t) = (2\pi)^{-3/2} \exp \left[i\mathbf{q} \cdot \mathbf{r} - \frac{i}{2} \int_{-\infty}^t (\mathbf{q} + \mathbf{A}(t'))^2 dt' \right], \quad (2.9)$$

are solutions to Eq. (2.7) in the length and velocity gauge, respectively. The wave functions of Eqs. (2.8) and (2.9) are known as Volkov wave functions. In Eqs. (2.8) and (2.9) we have assumed that the field is turned on adiabatically at $t = -\infty$ and we note that the Volkov solutions reduce to the usual plane waves in the absence of the field. In the single active electron approximation, we assume that the electronic state of the ion is unrelaxed, i.e., only ψ_N , the highest occupied molecular orbital (HOMO), is affected. The final state is then

$$\Psi_f = \frac{1}{\sqrt{N!}} \det | \psi_1(\mathbf{r}_1)\psi_2(\mathbf{r}_2)\dots\psi_V^{(c)}(\mathbf{r}_N,t) |_{R_0} \chi_{\nu_f}^+(R) e^{-iE_f^+ t}, \quad (2.10)$$

where superscripts “+” denote the ionic state. The time-averaged energy of the electron in the laser field is $q_n^2/2 + U_p$, with $U_p = F_0^2/(4\omega^2)$ being the ponderomotive or quiver energy which is the energy required for the electron to oscillate in the field. As the field strength increases, the quiver motion requires more energy to be maintained and in Sec. 2.4.3 we shall see that this increase in U_p leads to some interesting features. The total final state energy is

$$E_f = E_f^{e,+}(R_0^+) + E_{\nu_f}^+ + \frac{q_n^2}{2} + U_p, \quad (2.11)$$

where the final state momentum q_n is determined by energy conservation $n\omega = E_f - E_i$, i.e.,

$$q_n = \sqrt{2(n\omega - I_p^{\nu_f\nu_i} - U_p)}, \quad (2.12)$$

where we have defined the ionization potential

$$I_p^{\nu_f\nu_i} = E_f^{e,+}(R_0^+) + E_{\nu_f}^+ - E_i^e(R_0) - E_{\nu_i}, \quad (2.13)$$

between the vibrational states ν_i and ν_f , see Fig. 2.1. The transition amplitude of

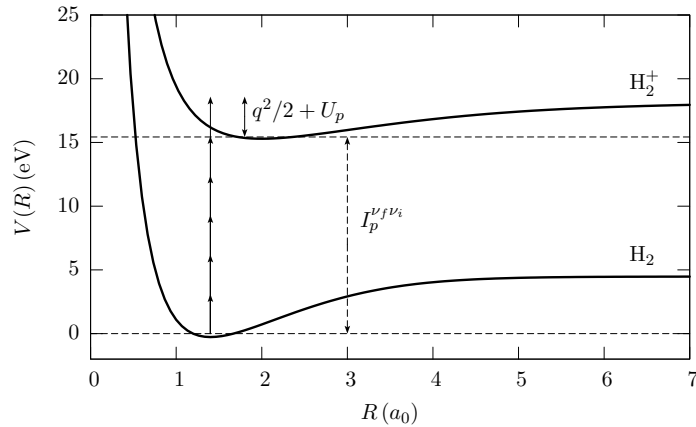


Figure 2.1: Potential curves for the lowest electronic states of H_2 and H_2^+ . The energies of the vibrational ground states of each of the electronic states are indicated by dashed lines. The excess energy from absorption of six photons at 400 nm goes to kinetic and quiver energy of the continuum electron.

Eq. (2.5) can now be written as ($c = \{\text{VG}, \text{LG}\}$)

$$A_{\mathbf{q}n}^{(c)} = \frac{1}{T} \int_0^T \langle \chi_{\nu_f}^+(R) \psi_V^{(c)}(\mathbf{r}_N, t) | V^{(c)}(t) | \psi_N(\mathbf{r}_N; R_0) \chi_{\nu_i}(R) \rangle \exp(iI_p^{\nu_f \nu_i} t) dt, \quad (2.14)$$

where the N -electron matrix element of the one-electron operators, Eqs. (2.1) and (2.2), has been simplified by the Slater-Condon rules [13]. The integration over nuclear coordinates can be performed immediately to give

$$A_{\mathbf{q}n}^{(c)} = S_{\nu_f, \nu_i} \frac{1}{T} \int_0^T \int [\psi_V^{(c)}(\mathbf{r}, t)]^* V^{(c)}(t) \psi_N(\mathbf{r}; R_0) d\mathbf{r}_N \exp(iI_p^{\nu_f \nu_i} t) dt, \quad (2.15)$$

where S_{ν_f, ν_i} is the Franck-Condon (FC) factor

$$S_{\nu_f, \nu_i} = \int [\chi_{\nu_f}^+(R)]^* \chi_{\nu_i}(R) dR. \quad (2.16)$$

The transition amplitude, Eq. (2.15), depends on the orientation of the molecule with respect to the field polarization. The electronic integral in Eq. (2.15) is most conveniently calculated in the laboratory fixed frame with a Z axis defined by the linear polarization axis. We may obtain the HOMO ψ_N in a *molecular* frame with standard quantum chemistry software [14, 15]. In order to evaluate the electronic integral we must rotate ψ_N properly according to the molecular orientation.

When the transition amplitude, Eq. (2.15), is inserted into Eq. (2.4), we obtain the ionization rate if one electron occupies the HOMO, however, we must take into account a possible degeneracy of the initial state. For molecules we multiply the rates by the number of equivalent electrons in the HOMO and for noble gas atoms with filled p shells we sum the rates from each magnetic sub-state to obtain the total rate of ionization.

2.1.1 Qualitative discussion of the effect of nuclear motion

The transition amplitude of Eq. (2.15) consists of two factors, namely the Franck-Condon (FC) factor and an electronic matrix element and both factors depend on the vibrational levels considered. The rates to each vibrational level are therefore not just proportional to the FC factors. Instead the relative populations in the lower final vibrational states are enhanced, compared with the distribution obtained from the FC factors alone, because the electronic matrix element is favoured by the smallest energy differences. When including vibrations, the total rate summed over all final vibrational states will therefore typically be smaller than if the vibrational ground state of the ion had been given the weight of unity.

The importance of the inclusion of nuclear vibrations will depend on the properties of the neutral molecule and the molecular ion. If their potential curves are only shifted in energy with respect to each other but otherwise exactly identical then the vibrational eigenstates will be identical too. The orthogonality of the nuclear wave functions then assures that only a single FC will be nonzero. We may estimate the importance of nuclear vibrations using molecular orbital theory and by considering the type of valence orbitals. If the valence orbital is nearly non-bonding as, e.g., in N_2 , the bonding properties of the molecular ion will be approximately equal to the bonding properties of neutral molecule and transitions between the vibrational ground states of the molecule and the ion dominate. In the case of a bonding HOMO as, e.g., in D_2 , the bonding of the ion will be weakened and transitions to many vibrational states will occur. We shall return to this point in Secs. 2.4.2 and 2.4.3.

2.2 Molecular tunneling theory

The molecular tunneling theory (MO-ADK) [16] is a generalization of the atomic Ammosov-Delone-Krainov (ADK) tunneling theory [10]. The physical idea behind the tunneling model is sketched in Fig. 2.2 which shows the potential seen by an electron in a potential generated from an atomic core and a static (DC) external field. The electron may tunnel through the barrier in the negative Z direction and the purpose of the tunneling theory is to determine the rate at which the tunneling occurs. The tunneling theory relies on the assumption that at any given instant of time the molecule will respond to the external laser field as if it were a static electric field. The rate of ionization in an oscillating field will then be determined by the time-averaged static rates. Whether this quasistatic approach is reasonable or not depends on the timescale of the ionization dynamics compared with the temporal variation of the field. A quantitative measure of the ratio of these timescales is the Keldysh parameter [7]

$$\gamma = \sqrt{2E_b} \frac{\omega}{F_0}, \quad (2.17)$$

which is the approximate duration of the ionization process divided by the optical period. In Eq. (2.17), E_b is the binding energy of the electron and the timescale of the ionization process is estimated as the time it takes for a classical electron with energy

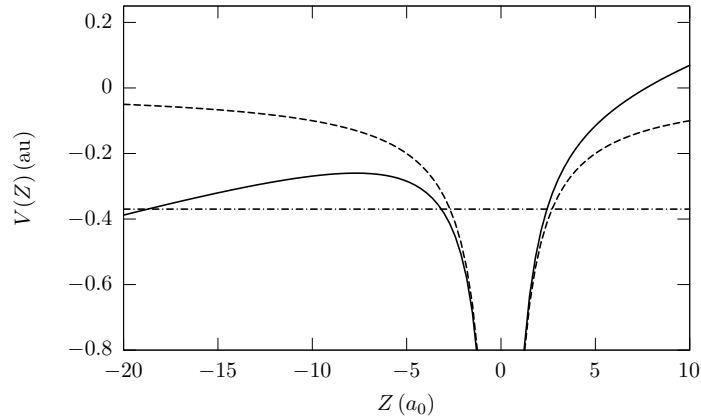


Figure 2.2: Sketch of the potential seen by an electron in a combined Coulomb potential and a static field directed along the Z axis (solid). The pure Coulomb potential (dashed) and the bound state energy (chain) is also shown.

E_b to travel a distance which is equal to the length of the barrier. The quasistatic regime is characterized by $\gamma \ll 1$.

The formulation of a tunneling theory in the case of molecules is complicated compared to the atomic case by two related features. Firstly, the presence of multiple nuclei within the molecule breaks the spherical symmetry of the field-free system and necessitates a description of the molecular wave function in terms of a superposition of partial waves. Secondly, the Euler angles describing the orientation between the laboratory fixed frame (with a Z -axis determined by the linear polarization vector of the external field) and the molecular body fixed frame have to be specified. Note that we use (X, Y, Z) to label the laboratory fixed frame of reference and (x, y, z) to label the body-fixed frame of reference. The tunneling rate of molecules can be determined once the field-free asymptotic wave function is known. In a body-fixed frame, labeled by superscript B , this function must follow the asymptotic Coulomb form

$$\psi_N^B(\mathbf{r}) \sim r^{Z_{\text{ion}}/\kappa-1} e^{-\kappa r} \sum_{l,m} C_{lm} Y_{lm}(\hat{\mathbf{r}}), \quad (2.18)$$

where Z_{ion} is the charge of the residual ion and κ is related to the binding energy, $\kappa = \sqrt{2E_b}$. We may verify that Eq. (2.18) is the correct asymptotic form by substitution into the Schrödinger equation with the long-range potential $-Z_{\text{ion}}/r$ and the energy $-E_b$. For the tunneling process in the DC case, we assume the electric field to point in the positive Z -direction, corresponding to a situation where tunneling would occur in the negative Z -direction. Consequently, we need to express the asymptotic form of the molecular wave function in that direction. If the body-fixed frame is rotated by the Euler angles (α, β, γ) with respect to the laboratory fixed system, the asymptotic form in the laboratory fixed system of the field-free molecular ground state wave function is expressed through the rotation operator $\hat{D}(\alpha, \beta, \gamma)$ as $\psi_N^L(\mathbf{r}) = \hat{D}(\alpha, \beta, \gamma)\psi_N^B(\mathbf{r})$, where

we have used the superscript L to denote the laboratory fixed system. Equation (2.18) then leads to the expression

$$\psi_N^L(\mathbf{r}) \sim r^{Z_{\text{ion}}/\kappa-1} e^{-\kappa r} \sum_{l,m} C_{lm} \sum_{m'} \mathcal{D}_{m'm}^{(l)}(\alpha, \beta, \gamma) Y_{lm'}(\hat{\mathbf{r}}), \quad (2.19)$$

where $\mathcal{D}_{m'm}^{(l)}(\alpha, \beta, \gamma)$ is a Wigner rotation function [17]. In Eq. (2.19) the sum over m' and the corresponding Wigner functions describes the rotation between the coordinate systems and the sum over l, m is a signature of the breaking of the spherical symmetry by the molecular system. For linear molecules the projection m of the electronic angular momentum onto the body-fixed axis is a good quantum number and, hence, for such systems there would be no summation over m in Eqs. (2.18) and (2.19). For later convenience, we note that α and γ represent rotations around the space-fixed Z -axis and the body fixed z -axis, respectively, while β is the angle between the Z and z axes.

From the asymptotic form of Eq. (2.19), the total ionization rate in a static (DC) field in the positive Z direction is calculated as in the atomic case [18–20]. In brief, the ionization rate is found as the flux of the probability current density, $j_z = (i/2)(\psi \partial_Z \psi^* - \psi^* \partial_Z \psi)$, through a surface element in the negative Z direction. An approximate expression for the wave function is found by considering the boundary conditions, namely that it should approximately be equal to the field-free asymptotic wave functions in the region under the barrier and it should be represented by a running wave solution outside the barrier. The wave function is now determined by a comparison of these two forms under the barrier and an analytical expression for the ionization rate is then obtained as

$$W_{\text{stat}}(F_0) = \sum_{m'} \frac{|B_{m'}|^2}{2^{|m'|} |m'|! \kappa^{2z/\kappa-1}} \left(\frac{2\kappa^3}{F_0} \right)^{2Z/\kappa-|m'|-1} \exp\left(-\frac{2}{3} \frac{\kappa^3}{F_0}\right), \quad (2.20)$$

where

$$B_{m'} = (-1)^{(|m'|+m')/2} \sum_{l,m} \sqrt{\frac{(2l+1)(l+|m'|)!}{2(l-|m'|)!}} C_{lm} \mathcal{D}_{m'm}^{(l)}(\alpha, \beta, \gamma). \quad (2.21)$$

In a slowly varying field, the ionization rate is found by averaging the DC rate over an optical cycle T

$$W = \frac{1}{T} \int_0^T W_{\text{stat}}(F_0 \cos(\omega t)) dt. \quad (2.22)$$

The DC rate is given by Eq. (2.20) when the field is oriented in the positive Z direction, $|\pi - \omega t| \geq \pi/2$, corresponding to tunneling in the negative Z -direction. When the field points in the negative Z direction, $\pi/2 \leq \omega t \leq 3\pi/2$, corresponding to the possibility for tunneling in the positive Z -direction, the geometry is equivalent to a field pointing in the positive Z direction but with an inverted molecule. We account for this by applying the parity operator \mathcal{P} on the wave function ψ_N^B

$$\mathcal{P} \psi_N^B(\mathbf{r}) \sim r^{Z_{\text{ion}}/\kappa-1} e^{-\kappa r} \sum_{l,m} C_{lm} (-1)^l Y_{lm}(\hat{\mathbf{r}}), \quad (2.23)$$

and we see by comparing with Eq. (2.18) that this simply corresponds to the substitution $C_{lm} \rightarrow (-1)^l C_{lm}$ in Eq. (2.21). Note that parity eigenstates, corresponding to molecules with inversion symmetry, contain only even or odd l states. When the field direction is changed Eq. (2.21) will either remain invariant or change sign and the rate, Eq. (2.20), is thereby left invariant. Contrary, the DC rate will not be invariant to field inversion for states which are not parity eigenstates. This is also to be expected since the wave functions in the tunneling regions in the positive and negative Z direction will be different. Under the assumption $\kappa^3/F_0 \ll 1$ the integral in Eq. (2.22) may be approximated by [20]

$$W = \sqrt{\frac{3F_0}{\pi\kappa^3} \frac{W_{\text{stat}}^+(F_0) + W_{\text{stat}}^-(F_0)}{2}}, \quad (2.24)$$

where $W_{\text{stat}}^\pm(F_0)$ are the DC rates for the positive and negative field directions with respect to the Z direction.

The tunneling theory gives an analytical expression for the total rate of ionization, Eqs. (2.20) and (2.24). We just need the numerical values for the asymptotic expansion coefficients, C_{lm} . Our procedure to find these coefficients is to match the HOMO from a Hartree-Fock calculation to the asymptotic form of Eq. (2.18) with C_{lm} as fitting parameters.

The tunneling theory can be extended to include effects of vibrations. In the quasistatic picture all potentials seen by the active electron should be regarded as being static. This means that the nuclei are fixed and the height of the tunneling barrier will depend on the internuclear distance chosen. We then calculate the rate for each value of R and weight these R -dependent rates by the probability distribution of R obtained from the nuclear wave function [16]. As will be demonstrated in Sec. 2.4.2 the effect of this R -dependent weighting is quite small.

2.3 Ion signal

In both theories discussed above we get an ionization rate corresponding to a field of constant amplitude, Eqs. (2.4) and (2.24). In a real laser pulse, however, the amplitude varies in time. Here we will simulate a laser pulse which amplitude variation is sufficiently slow so that at any given instant of time during the pulse, the field has approximately constant amplitude. We can then calculate an ionization probability by a proper integration of the rates which are obtained under the assumption of constant amplitude. This method is clearly inapplicable for a few-cycle pulse, where the amplitude varies significantly during an optical cycle. In this work we typically consider pulse lengths with 20 or more oscillations. In addition to the amplitude dependence, the rate also depends on the molecular orientation described by the Euler angles (α, β, γ) . We only consider linearly polarized light and hence the results are independent of α , the angle of rotation around the polarization vector. For a Gaussian laser beam with a Gaussian temporal profile with full width at half maximum τ , the amplitude of the

field is

$$F_0(\mathcal{R}, \mathcal{Z}, t) = \sqrt{I_0} \frac{w_0}{w(\mathcal{Z})} e^{-\mathcal{R}^2/w(\mathcal{Z})^2} \exp\left(-\frac{2 \ln 2t^2}{\tau^2}\right), \quad (2.25)$$

where $(\mathcal{R}, \mathcal{Z})$ are the cylindrical coordinates, I_0 the peak intensity, w_0 is the spot size and $w(\mathcal{Z}) = w_0 \sqrt{1 + \mathcal{Z}^2/\mathcal{Z}_R^2}$ where $\mathcal{Z}_R = \pi w_0^2/\lambda$ is the Rayleigh length and λ the wavelength.

The rate equations for the ionization probability of a molecule oriented according to the Euler angles (β, γ) and located at $(\mathcal{R}, \mathcal{Z})$ in the laser focus are

$$\frac{dp_0^{\nu_i}}{dt} = - \sum_{\nu_f} W^{\nu_f, \nu_i}(F_0(\mathcal{R}, \mathcal{Z}, t), \beta, \gamma) p_0^{\nu_i} \quad (2.26)$$

$$\frac{dp_1^{\nu_f}}{dt} = W^{\nu_f, \nu_i}(F_0(\mathcal{R}, \mathcal{Z}, t), \beta, \gamma) p_0^{\nu_i}, \quad (2.27)$$

where $p_0^{\nu_i}$ and $p_1^{\nu_f}$ denote the probabilities of having a neutral or an ion in the vibrational states ν_i and ν_f , respectively, and W^{ν_f, ν_i} denotes the rate between these vibrational states. We have assumed that only one vibrational state of the neutral is populated, and ionization to higher than singly charged ions is neglected. We can easily integrate Eq. (2.26) and by probability conservation, we find the total ionization probability to all vibrational states by the end of the pulse

$$p_1(\mathcal{R}, \mathcal{Z}, \beta, \gamma) = 1 - \exp\left[- \sum_{\nu_f} \int_{-\infty}^{\infty} W^{\nu_f, \nu_i}(F_0(\mathcal{R}, \mathcal{Z}, t'), \beta, \gamma) dt'\right]. \quad (2.28)$$

If the ionization probability is low $p_0^{\nu_i} \approx 1$, we can integrate Eq. (2.27) for each ν_f independently to get the ionization probability to each of the final vibrational states

$$p_1^{\nu_f}(\mathcal{R}, \mathcal{Z}, \beta, \gamma) \approx \int_{-\infty}^{\infty} W^{\nu_f, \nu_i}(F_0(\mathcal{R}, \mathcal{Z}, t'), \beta, \gamma) dt'. \quad (2.29)$$

The orientational dependent number of ionized molecules N_1 is found by integrating Eq. (2.28) over the beam profile

$$N_1(\beta, \gamma) = 2\pi\rho \int \mathcal{R}d\mathcal{R} \int d\mathcal{Z} p_1(\mathcal{R}, \mathcal{Z}, \beta, \gamma), \quad (2.30)$$

where ρ is the constant density of the target gas. A similar integration of Eq. (2.29) will of course lead to the number of ions in a definite vibrational state. In experiments it is difficult to measure the absolute yield due to unknown detection efficiency. The measured ion signal is, however, proportional to the number of ionized molecules. Relative measurements, e.g., measurements on ratios of yields for different molecular orientations are thus independent of detection efficiency.

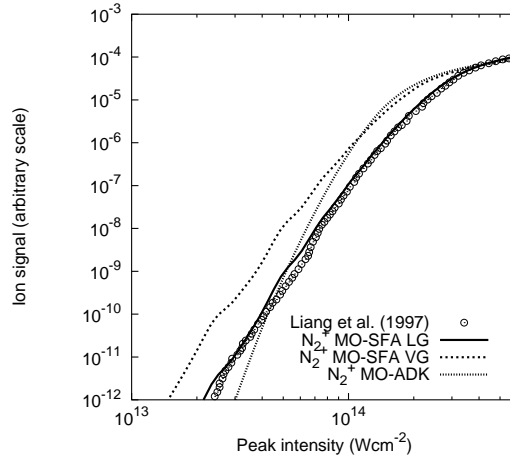


Figure 2.3: Ion signal versus peak intensity for single ionization from N_2 . The laser wavelength is 800 nm, the pulse duration (FWHM) is 250 fs and the beam waist $98 \mu\text{m}$. The theoretical predictions of the length gauge MO-SFA (solid), the velocity gauge MO-SFA (long-dashed) and the MO-ADK (short-dashed) are also shown. The experimental data points are from Ref. [21].

2.4 Results

The typical ionization experiment of the late nineties was to shoot in an intense laser into a thin gas of molecules. The ions created would be extracted from the interaction region by a time-of-flight spectrometer and the total number of ions with a desired charge to mass ratio could be measured. Figure 2.3 shows a typical result of such an experiment which measures the number of N_2^+ ions created from an N_2 target gas. At first sight the agreement between the theories and experiment looks quite satisfactory. However, one should keep in mind that the signal is integrated over all directions and energies of the outgoing electron, averaged over all molecular orientations and integrated over the spatial and temporal pulse profile. Furthermore, the ion signal is recorded on an arbitrary scale due to unknown target pressure and detection efficiency and the data points can be displaced vertically in order to take into account this arbitrariness. Clearly, some information is lost when integrating the signal and in order to gain more detailed information on the ionization dynamics more elaborate experiments have been performed recently. In the following sections we shall discuss some of these experiments and test the quality of the approximate models against the experimental results. These sections contain a summary of the papers [2, 4, 5].

2.4.1 Orientational dependent ionization

The usual experimental setup utilizes a randomly oriented ensemble of target molecules. In order to make a comparison to theory one then has to average the calculated signals over the orientation which are parameterized by the angles (β, γ) , Eq. (2.30). The

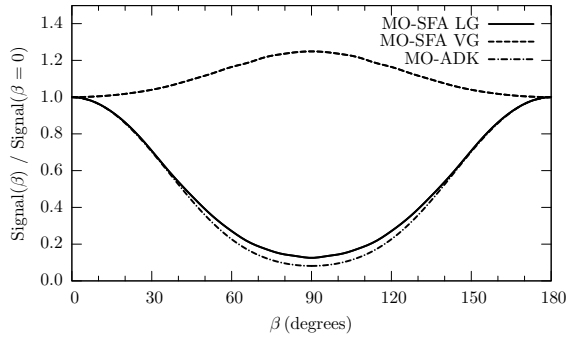


Figure 2.4: Calculated ion signal for different orientations between the polarization axis and the internuclear axis described by the angle β . For $\beta = 0^\circ$ the polarization vector is along the molecular axis. The figure shows results from the models: length gauge MO-SFA (MO-SFA LG, solid), velocity gauge MO-SFA (MO-SFA VG, dashed) and MO-ADK (chain). The peak intensity is $2 \times 10^{14} \text{ Wcm}^{-2}$, the pulse duration (FWHM) 40 fs and the wavelength 800 nm. These values are chosen to match experimental values of Ref. [22].

anisotropy of a molecule suggests that ionization as well as rescattering would depend on how the molecule is oriented with respect to the field direction. Recent progress in the ability to align molecules has made it possible to measure orientational dependent ionization signals [22]. More specifically, ion signals of N_2^+ were measured when the molecules were aligned preferentially parallel and perpendicular to the field polarization. This experiment revealed that N_2 is approximately four times more likely to ionize when aligned parallel to the field compared to the perpendicular alignment. In Fig. 2.4 the predicted ion signal is plotted as a function of the angle β between the internuclear axis and the laser polarization. The angle γ which describes rotations around the body fixed axis contains no information for the linear N_2 molecule and can arbitrarily be set equal to zero. The behaviour of the length and velocity gauge SFA curves is completely reverse. In the velocity gauge, the rate and signal is maximized when the molecule is aligned perpendicular to the field direction. Contrary, and in accordance with experimental findings [22], the length gauge MO-SFA and the MO-ADK theory strongly favour the parallel alignment.

When comparing the results obtained in the velocity and length gauges in Fig. 2.4, it is clear that the MO-SFA length gauge and the MO-ADK results account for the trend in the experimental data. From the form of the length gauge interaction of Eq. (2.2) it is clear that $V^{(\text{LG})}(t)$ favours large distances in coordinate space. For N_2 the coordinate space wave function (HOMO) and charge density is maximized along the internuclear axis (Fig. 2.5) and the maximum rate in the length gauge is thus expected to correspond to the parallel geometry. Of course this argument also accounts for the tunneling results since the tunneling rate depends on the asymptotic wave function in the field direction. Comparison with the experiment indicates that the wave function at large distances is the important part of the configuration space for this process. As

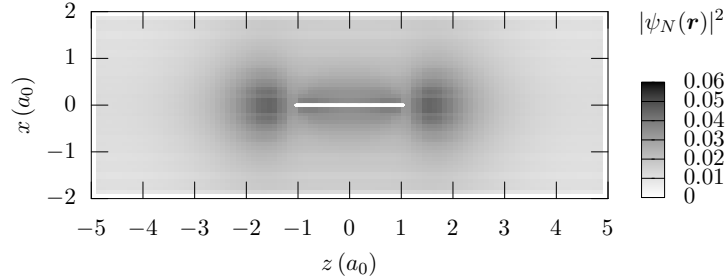


Figure 2.5: Probability density of the electron which occupies the HOMO of N_2 . The internuclear axis (white) is directed along the z axis.

	Ar	D ₂	N ₂	Xe	O ₂
Ionization potential (eV)	15.76	15.43	15.58	12.13	12.06

Table 2.1: Ionization potentials of diatomic molecules and companion atoms. The molecular ionization potentials are measured between the vibrational ground states $\nu_i = \nu_f = 0$.

seen from Eq. (2.1), $V^{(\text{VG})}(t)$ probes regions of space where the wave function varies rapidly with distance, i.e., regions close to the nuclei. The failure of the velocity gauge MO-SFA to account for the trend in the experimental data suggests that this probing of short distances leads to an overestimation of the molecular ground state properties compared to the influence of the external field.

2.4.2 Diatomic molecules and companion atoms

The atomic tunneling theory has been very successful in describing the ionization rates of atoms. This theory depends primarily on the ionization potential. If the ionization potential is the only important quantity one would expect similar ionization rates for molecules and atoms with similar ionization potentials, the so-called companion atoms. To address this proposal, several experiments measuring the ratio of ion yields of diatomic molecules and their companion atoms [21, 23–27]. The ratiometric measurements are illuminating since effects are factored out which depend only on the binding energy. Hence a comparison of the ratio of ionization signal of, e.g., N_2 and its companion Ar atom allows one to study fairly directly effects of molecular symmetry and ro-vibrational motion. The experiments have revealed that some molecules are harder to ionize than their companion atoms, a phenomena which is known as suppressed ionization.

In Fig. 2.6 the experimental results and the theoretical predictions are summarized. The theoretical predictions are nearly independent of the pulse length and thus experiments with different pulse durations can be compared with the same theoretical

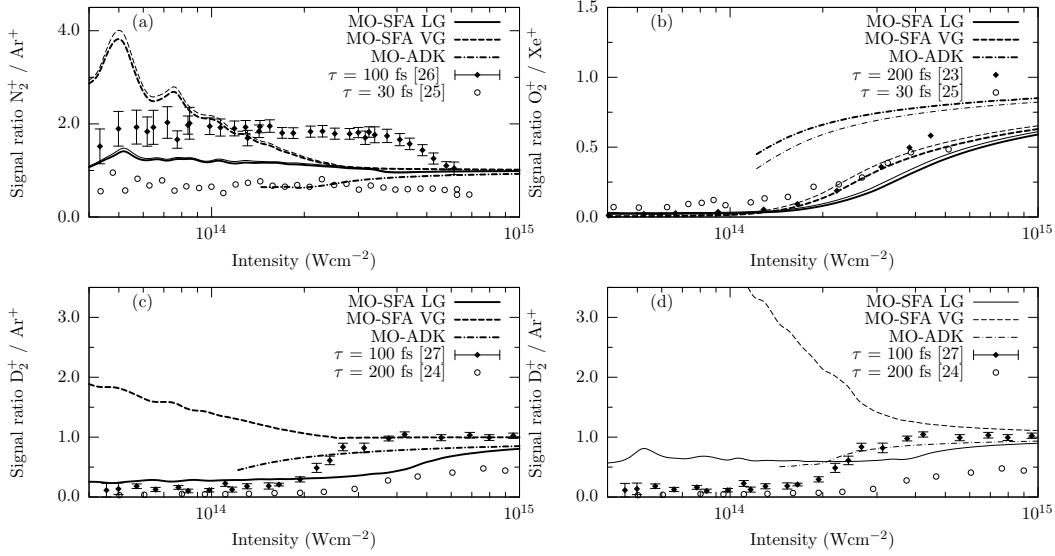


Figure 2.6: Intensity dependent ratios between the ion yields of (a) $N_2^+ : Ar^+$, (b) $O_2^+ : Xe^+$, and (c)-(d) $D_2^+ : Ar^+$. In all panels the laser wavelength is 800 nm and for the theoretical calculations the pulse duration is 100 fs. The thin lines are calculations with fixed nuclei and the thick lines are the corresponding calculations including vibrations. The fixed nuclei (c) and vibrating nuclei calculations (d) are separated for $D_2^+ : Ar^+$ to ease readability.

curves. First of all, we note that the different experiments do not agree very well. The only difference between the experiments is the pulse duration and one proposal for this dependence is that molecules can align themselves during the pulse through the interaction of the field with the molecular polarizability. Such an alignment effect would be larger for a longer pulse duration and we have already seen in Sec. 2.4.1 that the ion yield of aligned molecules can be significantly different from randomly orientated molecules. However, even for the longest pulses considered here, the pulse duration is too short for such a dynamical alignment to occur [16] and the molecular ensemble should always be regarded as being randomly oriented. For this reason we then tend to conclude that the experimental discrepancies are due to experimental uncertainties. A complete quantitative comparison between experiments and the theoretical models is then impossible and we will restrict our comparison to the qualitative features which are shared between the experiments.

From a qualitative point of view, the experiments do agree that N_2 and its companion atom Ar are approximately equally likely to ionize, Fig. 2.6 (a), while both O_2 and D_2 , Figs. 2.6 (b)-(c), are harder to ionize than their atomic counterparts. At high intensities both the atomic and molecular signals saturate, i.e., the peak intensity becomes so high that the ionization probability in the laser focus is nearly 100% for both species. When such saturation effects become important, the ratio approaches unity. For all three molecular-atomic pairs, we show the predictions of the theoretical models

with inclusion of nuclear vibrations and with fixed nuclei. The MO-ADK model can only be meaningfully applied when the Keldysh parameter, Eq. (2.17), fulfils $\gamma \leq 1$ and hence, we only show the MO-ADK results in the intensity range where this requirement is fulfilled. All models do correctly predict absence of suppressed ionization for $\text{N}_2:\text{Ar}$ and presence of suppressed ionization for $\text{O}_2:\text{Xe}$. For the N_2 and O_2 molecules we note that inclusion of nuclear vibrations has only minor effects on the results.

For $\text{D}_2:\text{Ar}$ we find absence of suppressed ionization when we use the MO-SFA VG model which is clearly in contradiction with experimental data. On the other hand the MO-SFA LG and MO-ADK models both correctly predict suppression. The MO-SFA LG model has some problems in reproducing the intensity at which saturation occurs and the ratio approaches unity. We note that the experiments do not agree on the saturation intensity either. The longer pulse length should be equivalent to a lower saturation intensity but this is clearly not the case when comparing the two sets of experimental data in Fig. 2.6 (c). We see that the inclusion of nuclear vibrations [Fig. 2.6 (c)] reduce the MO-SFA ratios by a significant factor compared with the fixed nuclei calculations [Fig. 2.6 (d)]. The origin of this effect was discussed in Sec. 2.1.1. The point is simply that the inclusion of vibrational motion will reduce the rate when the molecule and the molecular ion have different bonding properties and transitions to many different vibrational states occur.

In summary we find a rather good overall agreement between the MO-SFA LG theory and experiments on diatomic molecules and their companion atoms, and we believe that the MO-SFA LG model accounts quite well for the structural dependence on the strong-field ionization rates. In general we find the length gauge MO-SFA to be in better agreement with experiments than the velocity gauge MO-SFA – in particular in the case of $\text{D}_2:\text{Ar}$ where the MO-SFA VG predicts no suppression of ionization in contradiction with the experimental findings and the other theories. Quantitative comparisons are difficult due to disagreements between different experiments, and further experiments would therefore be highly desirable.

2.4.3 Vibrational distributions

In this section we will investigate further the partitioning of energy among the electronic and nuclear degrees of freedom when ionizing a diatomic molecule by a strong laser field. This is a topic of much current interest: until recently it was assumed that the distribution of vibrational states formed in the molecular ion following ionization of the neutral molecule follows a Franck-Condon (FC) distribution (see [28] and references therein). A recent experiment, however, reported a non-FC distribution and suggested that the use of the FC principle is inaccurate because the rate for tunneling ionization increases sharply with internuclear distance [28]. We will show that the rapid response of the electron to the laser field in fact ensures the applicability of the FC principle for the nuclear motion at each instant of time during the pulse. It is instead the variation of the ionization and excitation rate with intensity in the focal volume that leads to a departure from a conventional FC-like distribution.

Throughout this section we will only use the length gauge molecular strong field

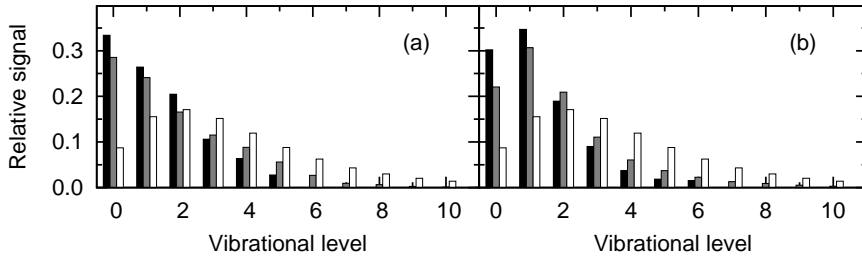


Figure 2.7: The vibrational distribution of H_2^+ after ionization in an intense laser field. The black bars indicate the experimental observations [28] and the gray bars are the predictions according to the present theory. The Franck-Condon distribution is indicated with white bars. In both panels the laser wavelength is 800 nm, the pulse duration (full width at half maximum) is 45 fs. The peak laser intensities are (a) $3.0 \times 10^{13} \text{ Wcm}^{-2}$ and (b) $4.8 \times 10^{13} \text{ Wcm}^{-2}$.

approximation since this model has proven to produce the most reliable results in Secs 2.4.1 and 2.4.2.

In Fig. 2.7, we present the experimental and theoretical vibrational distribution of H_2^+ produced by strong-field ionization of H_2 for two different intensities. For comparison also squared FC factors are shown. At both intensities, we find good agreement between experiment and theory. Both distributions favor the lower vibrational states in contrast to the FC distribution.

Even though the FC principle is explicitly used in our theory [see Eq. (2.15)], the predicted and observed vibrational distributions deviate significantly from the FC distribution. The key concept explaining this discrepancy is the effect of channel closings in connection with full account of the pulse profile. By energy conservation, Eq. (2.12), the number of absorbed photons n must fulfil the criterion $n\omega \geq I_p^{\nu_f \nu_i} + U_p$ with $I_p^{\nu_f \nu_i}$ being the ionization potential to the level ν_f from the vibrational ground state $\nu_i = 0$, which is the only vibrational state initially populated. The presence of $U_p = F_0^2/(4\omega^2)$ means that the minimum number of photons needed to reach the electronic continuum and a particular vibrational state ν_f in the ion increases with intensity. This phenomena is referred to as channel closing and the effect is illustrated in Fig. 2.8, where we show the ionization rates to the lowest vibrational levels of H_2^+ when ionizing molecules aligned parallel to the laser field at a wavelength of 800 nm. At an intensity of $1 \times 10^{13} \text{ Wcm}^{-2}$ all the vibrational states shown can be reached by absorption of 11 photons. As the intensity increases the thresholds shift upwards by U_p and at the intensities marked by arrows, absorption of 11 photons becomes insufficient to reach the vibrational levels indicated. For example, in the intensity range of $2.3 - 2.7 \times 10^{13} \text{ Wcm}^{-2}$ one needs $n \geq 12$ photons to reach the $\nu_f \geq 1$ levels whereas $n = 11$ is sufficient for $\nu_f = 0$. Since the rates for higher order processes ($n \geq 12$) are much lower than the rate for $n = 11$, this explains why the $\nu_f = 0$ is favored by a factor of 3 over $\nu_f = \{1, 2\}$ in Fig. 2.8. Contrary, when the same number of photons is needed to reach all ν_f levels, the rate to $\nu_f = 0$ is generally lower than to $\nu_f = \{1, 2\}$ due to the smaller FC factor of the former.

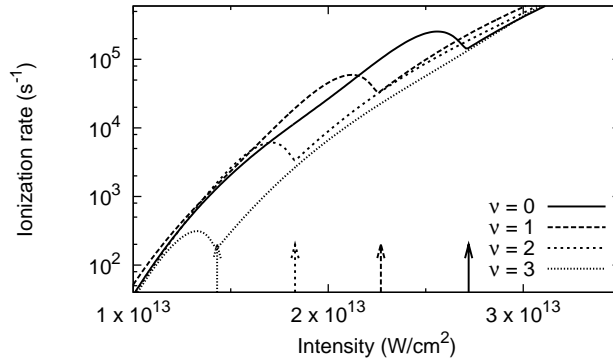


Figure 2.8: Ionization rates to the lowest vibrational states of H_2^+ from H_2 molecules aligned parallel to the laser field at the wavelength of 800 nm. Note logarithmic scale.

The reason for finding a very different relative relationship between the *signals* at the peak intensity of $3 \times 10^{13} \text{Wcm}^{-2}$, Fig. 2.7 (a), and the *rates* at the same intensity is a result of taking the pulse shape into account. Only in the very center of the Gaussian laser beam the intensity reaches the peak intensity. In other regions of space the molecules are exposed to a lower intensity and excitation to $\nu_f = 0$ dominates.

So far we have seen that the vibrational distribution depends remarkably on the intensity. Our next purpose is to investigate how the laser pulse can be shaped to maximize the population in a given vibrational state. A high degree of population transfer to a definite state will be a valuable result as it will allow for the possibility of making state-specific experiments on the molecular ion. To our knowledge, such type of control has not previously been explored in strong-field physics. We have chosen to shape the pulse by a simple variation of the peak intensity with the purpose of maximizing the $\nu_f = 0$ population. We have performed the optimization at the wavelengths corresponding to the fundamental- and frequency doubled wavelengths of the Ti:Sapphire (400 nm and 800 nm) laser. During the optimization, the pulse duration is fixed at 45 fs.

The result of the intensity optimization is shown in Fig. 2.9. At the shortest wavelength, 400 nm, a relative population as large as 75% is produced in the vibrational ground state at an intensity of $2 \times 10^{12} \text{Wcm}^{-2}$. In our model, the reason for obtaining such a confined distribution is that the ion yield is completely dominated by 5-photonabsorption which is only possible to the $\nu_f = 0$ state. At the longer wavelength the selection of the $\nu_f = 0$ becomes less efficient. The decreasing $\nu_f = 0$ population with increasing wavelength was also observed experimentally [29, 30], and the general phenomenon that the largest population in the vibrational ground state is obtained at relatively low intensities is in good agreement with the experiments.

The vibrational wave functions of H_2 and H_2^+ lead to a quite broad FC distribution and accordingly many vibrational states are populated after ionization. If one considers molecules where only a few FC factors are important, one may hope for a more efficient

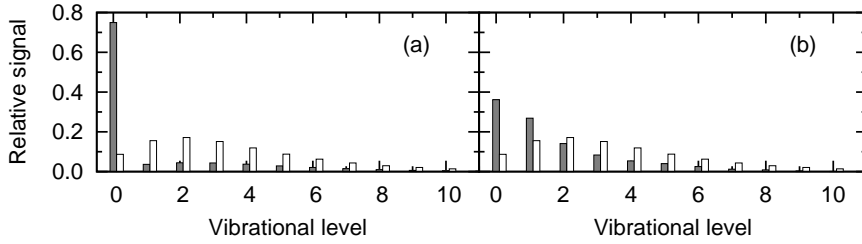


Figure 2.9: The vibrational distribution of H_2^+ after ionization in an intense laser field according to the present theory (gray bars). The Franck-Condon distribution is indicated with white bars. The peak laser intensity is chosen to maximize the population in the lowest vibrational state. The laser wavelengths are (a) 400 nm, and (b) 800 nm, and the peak intensities are (a) $2.0 \times 10^{12} \text{ Wcm}^{-2}$, and (b) $2.6 \times 10^{13} \text{ Wcm}^{-2}$. In both panels the pulse duration is 45 fs.

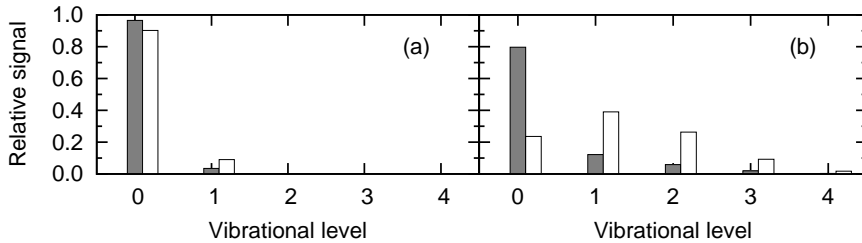


Figure 2.10: The vibrational distribution of N_2^+ (a) and O_2^+ (b) after ionization in an intense laser field according to the present theory (gray bars). The Franck-Condon distributions are indicated with white bars. In both panels the laser wavelength is 800 nm and the pulse duration is 45 fs. Maximization of the population in the lowest vibrational state is obtained with the peak intensities of (a) $2.4 \times 10^{13} \text{ Wcm}^{-2}$ for N_2^+ , and (b) $3.6 \times 10^{12} \text{ Wcm}^{-2}$ for O_2^+ .

optimization. To this end, we now investigate ionization of N_2 and O_2 where the number of final vibrational states are limited to $\nu_f \leq 1$ and $\nu_f \leq 4$, respectively, simply because the other FC factors are vanishingly small. In Fig. 2.10 we show the optimized distributions for N_2 and O_2 at a wavelength of 800 nm. For N_2 , only two states will be populated in N_2^+ and we see that the FC factors strongly favour the $\nu = 0$ state (90%). If we use an optimized laser intensity we may reach a $\nu = 0$ population of 97% [Fig. 2.10 (a)]. In Fig. 2.10 (b) we present the results for O_2 and we see that an efficient selection of the $\nu = 0$ state can also be obtained for this molecule. We find the optimal population to be 80% compared with the FC distribution of 24%. When we compare the results of N_2 and O_2 with the results of H_2 at the same wavelength [Fig. 2.9 (b)], we see that the former molecules can indeed be brought to the $\nu = 0$ state more efficiently due to the limited number of final vibrational states.

3. Exact one-electron solution

In this section we will demonstrate how the dynamics of one electron can be solved by integration of the time dependent Schrödinger equation. The integration is performed in discrete time steps and the wave function is represented in a finite basis. The solution will converge towards the exact solution in the limit of infinitely small time steps and infinitely large basis.

3.1 The split step method

We wish to solve the three-dimensional time dependent Schrödinger equation of an electron in a time dependent potential

$$i\frac{\partial}{\partial t}\Psi(\mathbf{r}, t) = \left(-\frac{1}{2}\nabla^2 + V(\mathbf{r}, t)\right)\Psi(\mathbf{r}, t). \quad (3.1)$$

Here we assume that the time dependent potential $V(\mathbf{r}, t)$ is diagonal in space representation. We will use the spherical system of coordinates $\mathbf{r} = (r, \theta, \phi)$ and we introduce the reduced wave function $\Phi(\mathbf{r}, t) = r\Psi(\mathbf{r}, t)$. Equation (3.1) may then be rewritten

$$i\frac{\partial}{\partial t}\Phi(\mathbf{r}, t) = \left(-\frac{1}{2}\frac{\partial^2}{\partial r^2} + \frac{L^2}{2r^2} + V(\mathbf{r}, t)\right)\Phi(\mathbf{r}, t), \quad (3.2)$$

where L^2 is the usual angular momentum operator. Suppose the wave function is known at a time t . We propagate the wave function by the time evolution operator $\mathcal{U}(t + \Delta t, t)$ to obtain the wave function at a later time $t + \Delta t$. Equation (3.2) suggests the propagator

$$\mathcal{U}(t + \Delta t, t) = e^{i\Delta t\frac{1}{2}\frac{\partial^2}{\partial r^2}} \times e^{-i\Delta t\frac{L^2}{2r^2}} \times e^{-i\Delta tV(\mathbf{r}, t)} + \mathcal{O}(\Delta t^2). \quad (3.3)$$

The error term arises from the factorization of an operator exponential of non-commuting operators. The error term proportional to Δt^2 can be eliminated if we split the non-commuting operators in the following way

$$\mathcal{U}(t + \Delta t, t) = e^{i\frac{\Delta t}{2}\frac{1}{2}\frac{\partial^2}{\partial r^2}} \times e^{-i\frac{\Delta t}{2}\frac{L^2}{2r^2}} \times e^{-i\Delta tV(\mathbf{r}, t)} \times e^{-i\frac{\Delta t}{2}\frac{L^2}{2r^2}} \times e^{i\frac{\Delta t}{2}\frac{1}{2}\frac{\partial^2}{\partial r^2}} + \mathcal{O}(\Delta t^3). \quad (3.4)$$

The usual strategy for applying this propagator is to successively represent the wave function in representations that diagonalize the part of the Hamiltonian which is used for propagation.

As our starting point we will represent the angular part of the wave function in a finite number of spherical harmonics and the radial part on n_r equidistant radial grid points r_i between 0 and r_{\max} . The number of spherical harmonics is truncated by a maximum l_{\max} quantum number which is chosen large enough such that higher excited angular momentum states can safely be neglected.

$$\Phi(\mathbf{r}, t) = \sum_{l=0}^{l_{\max}} \sum_{m=-l}^l f_{lm}(r_i, t) Y_{lm}(\hat{\mathbf{r}}). \quad (3.5)$$

Below we will use the shorthand notation \sum_{lm} for the double summation in Eq. (3.5). We see that the radial kinetic operator $-(1/2)\partial^2/\partial r^2$ acts only on the radial functions $f_{lm}(r, t)$ and it will act on each of these components independently. It is now convenient to write each of the radial functions in a discrete Fourier expansion

$$f_{lm}(r_i, t) = \sum_{k=0}^{n_r-1} g_{k,lm}(t) e^{\pi i k r_i / r_{\max}}, \quad (3.6)$$

where the expansion coefficients $g_{k,lm}(t)$ are given by

$$g_{k,lm}(t) = \frac{1}{n_r} \sum_{i=0}^{n_r-1} f_{lm}(r_i, t) e^{-\pi i k r_i / r_{\max}}. \quad (3.7)$$

When the radial functions are represented in the form of Eq. (3.6), it is easy to apply the radial kinetic operator

$$e^{i \frac{\Delta t}{2} \frac{1}{2} \frac{\partial^2}{\partial r^2}} f_{lm}(r_i, t) = \sum_{k=0}^{n_r-1} e^{i \frac{\Delta t}{2} \frac{1}{2} (\pi i k / r_{\max})^2} g_{k,lm}(t) e^{\pi i k r_i / r_{\max}}. \quad (3.8)$$

We return to the new radial functions $f_{lm}(r_i, t + \Delta t/2)$ by applying the transformation Eq. (3.6) with the propagated Fourier coefficients $g_{k,lm}(t + \Delta t/2) = e^{i \frac{\Delta t}{2} \frac{1}{2} (\pi i k / r_{\max})^2} g_{k,lm}(t)$.

The representation of Eq. (3.5) diagonalizes the centrifugal operator $L^2/(2r)$, such that

$$e^{-i \frac{\Delta t}{2} \frac{L^2}{2r^2}} \sum_{lm} f_{lm}(r_i, t) Y_{lm}(\hat{\mathbf{r}}) = \sum_{lm} e^{-i \frac{\Delta t}{2} \frac{l(l+1)}{2r_i^2}} f_{lm}(r_i, t) Y_{lm}(\hat{\mathbf{r}}), \quad (3.9)$$

i.e., by propagating the centrifugal term each radial function acquires a phase

$$f_{lm}(r_i, t + \Delta t/2) = e^{-i \frac{\Delta t}{2} \frac{l(l+1)}{2r_i^2}} f_{lm}(r_i, t). \quad (3.10)$$

The last operator to be used for propagation is the potential which is diagonal in space representation. The spatial wave function may be constructed on a grid point $\mathbf{r}_{ijk} = (r_i, \theta_j, \phi_k)$ from a discrete spherical harmonics synthesis. The effect of the potential is then

$$e^{-i \Delta t V(\mathbf{r}, t)} \Phi(\mathbf{r}_{ijk}, t) = e^{-i \Delta t V(\mathbf{r}_{ijk}, t)} \Phi(\mathbf{r}_{ijk}, t) \quad (3.11)$$

We recover the original form of Eq. (3.5) by a spherical harmonics decomposition of the propagated wave function.

The full time propagation of Eq. (3.4) is completed by application of the centrifugal- and radial kinetic operator once again.

The transformation scheme between the three representations was previously applied in two- [31] and three dimensions [32]. The main computational tasks lie in the construction of the spatial wave function from the spherical harmonics synthesis and in the subsequent spherical harmonics decomposition. Additionally, these transformations seem to be slightly unstable in the presence of singular potentials. In this light, it is of great interest to explore alternative propagation methods for the potential.

3.2 Propagation in the spherical harmonics basis

In this section, we will discuss how the spherical harmonics transformations can be avoided by propagating the potential in a non-diagonal representation. Our basic strategy will be to propagate the potential with the wave function represented in the form of Eq. (3.5). Suppose we have chosen some maximum l_{\max} quantum number. The number of spherical harmonics basis functions is then $n_{Y_{l_m}} = (l_{\max} + 1)^2$. For each fixed radial coordinate r_i we may write the potential as an $n_{Y_{l_m}} \times n_{Y_{l_m}}$ matrix in the spherical harmonics basis with the matrix elements

$$V_{l'm',lm}(r_i, t) = \langle l'm' | V(\mathbf{r}(r_i, \hat{\mathbf{r}}), t) | lm \rangle. \quad (3.12)$$

The brackets denote an integration over the angles $\hat{\mathbf{r}}$ and $|lm\rangle \equiv Y_{lm}(\hat{\mathbf{r}})$. Since we need to apply the operator $e^{-i\Delta t V(\mathbf{r}, t)}$, we must exponentiate the matrix which represents the potential. We may diagonalize the Hermitian matrix $\mathbf{V}(r_i, t)$ by a unitary matrix \mathbf{U}

$$\mathbf{V}(r_i, t) = \mathbf{U}(r_i, t) \cdot \mathbf{d}(r_i, t) \cdot \mathbf{U}^\dagger(r_i, t), \quad (3.13)$$

where $\mathbf{d}(r_i, t)$ is a diagonal matrix containing the real eigenvalues of $\mathbf{V}(r_i, t)$. The matrix representation of $e^{-i\Delta t V(\mathbf{r}, t)}$ is then

$$e^{-i\Delta t \mathbf{V}(r_i, t)} = \mathbf{U}(r_i, t) \cdot e^{-i\Delta t \mathbf{d}(r_i, t)} \cdot \mathbf{U}^\dagger(r_i, t). \quad (3.14)$$

$e^{-i\Delta t \mathbf{d}(r_i, t)}$ is a diagonal matrix with the elements

$$\left[e^{-i\Delta t \mathbf{d}(r_i, t)} \right]_{jj} = e^{-i\Delta t d_{jj}(r_i, t)}. \quad (3.15)$$

From Eq. (3.5) we see that the wave function can be written as a vector $\mathbf{f}(r_i, t)$ in the spherical harmonics basis for the fixed value of r_i . The effect of the operator $e^{-i\Delta t V(\mathbf{r}, t)}$ simply translates into a matrix multiplication

$$e^{-i\Delta t V(r_i, \hat{\mathbf{r}}, t)} \Phi(r_i, \hat{\mathbf{r}}, t) \doteq e^{-i\Delta t \mathbf{V}(r_i, t)} \cdot \mathbf{f}(r_i, t) \quad (3.16)$$

$$= \mathbf{U}(r_i, t) \cdot e^{-i\Delta t \mathbf{d}(r_i, t)} \cdot \mathbf{U}^\dagger(r_i, t) \cdot \mathbf{f}(r_i, t). \quad (3.17)$$

“ \doteq ” means that the right hand side is a matrix representation in the spherical harmonics basis. The result of these matrix multiplications is a vector which elements are the propagated coefficients $f_{lm}(r_i, t + \Delta t)$.

In general, the algorithm as it is described above is more computationally costly than the spherical harmonics synthesis and decomposition. The latter transformations have been demonstrated to require $8l_{\max}^4$ floating point operations [33]. By the present method, we must construct the matrix elements of the potential, Eq. (3.12), in each time step. Secondly, the matrix must be diagonalized and at last the three matrix multiplications of Eq. (3.17) must be performed. Diagonalization of an $n_{Y_{l_m}} \times n_{Y_{l_m}}$ matrix can be accomplished in $n_{Y_{l_m}}^3 \approx l_{\max}^6$ operations, i.e., significantly more than number of operations required to make the spherical harmonics synthesis and decomposition. If, however, the potential shows some symmetry, the computational effort can be greatly reduced as we shall demonstrate below.

3.2.1 H_2^+ in a time dependent linearly polarized electric field

In this example we will discuss our method of propagating the potential for a homonuclear molecule in a time dependent linearly polarized electric field $\mathbf{F}(t)$. For definiteness we choose the hydrogenic molecular ion with the two nuclei fixed in space at $\pm \mathbf{R}/2$. For the field-electron interaction we will assume that the dipole approximation applies. The problem is truly three-dimensional if we consider a geometry with the polarization axis rotated at an angle β with respect to the internuclear axis.

The potential may be split into a molecular time independent term $V^M(\mathbf{r})$ arising from the static nuclear attraction and a time dependent term $V^F(\mathbf{r}, t)$ caused by the field interaction

$$V(\mathbf{r}, t) = V^M(\mathbf{r}) + V^F(\mathbf{r}, t) \quad (3.18)$$

$$= -\frac{1}{|\mathbf{r} - \mathbf{R}/2|} - \frac{1}{|\mathbf{r} + \mathbf{R}/2|} + \mathbf{F}(t) \cdot \mathbf{r}. \quad (3.19)$$

Here we have chosen the length gauge field-electron interaction. Since the two terms in the potential mutually commute, we may factorize the exponential without any errors

$$e^{-i\Delta t V(\mathbf{r}, t)} = e^{-i\Delta t V^M(\mathbf{r})} e^{-i\Delta t V^F(\mathbf{r}, t)}. \quad (3.20)$$

We will now investigate the propagation of each of the two potentials in some detail.

The static molecular potential

Since the molecular potential is independent of time, we only need to evaluate its exponentiated matrix representation once and for all and subsequently store it in memory. The propagation with this term thus reduces to a single matrix multiplication in each time step. Furthermore, the symmetry of the potential imposes some selection rules on the matrix elements, so that a full matrix multiplication can be avoided.

We will orient the molecular axis along the z -axis and express $V^M(\mathbf{r})$ as

$$V^M(\mathbf{r}) = -\frac{1}{|\mathbf{r} - \mathbf{R}/2|} - \frac{1}{|\mathbf{r} + \mathbf{R}/2|} \quad (3.21)$$

$$= -\sum_L \frac{r_{<}^L}{r_{>}^{L+1}} P_L(\cos \theta) - \sum_L \frac{r_{<}^L}{r_{>}^{L+1}} P_L(-\cos \theta) \quad (3.22)$$

$$= -2 \sum_{L \text{ even}} \frac{r_{<}^L}{r_{>}^{L+1}} P_L(\cos \theta) \quad (3.23)$$

$$= -2 \sum_{L \text{ even}} \sqrt{\frac{2L+1}{4\pi}} \frac{r_{<}^L}{r_{>}^{L+1}} Y_{L0}(\cos \theta), \quad (3.24)$$

where $r_{<}$ ($r_{>}$) is the smaller (larger) of $(r, R/2)$. In the third line we have used that the L 'th Legendre polynomial has the parity $(-1)^L$. The matrix elements can now be

written as

$$V_{l'm',lm}^M(r_i) = -2 \sum_{L \text{ even}} \sqrt{\frac{2L+1}{4\pi}} \frac{r_{<}^L}{r_{>}^{L+1}} \langle l'm' | Y_{L0}(\cos \theta) | lm \rangle. \quad (3.25)$$

The integral over the three spherical harmonics is known as a Gaunt coefficient and is analytically known in terms of Clebsch-Gordan coefficients. From the angular part we find two selection rules

- The potential is azimuthally symmetric and cannot connect different m states, i.e., $V_{l'm',lm}^M(r_i) = 0$ unless $m' = m$.
- The potential is an even parity eigenstate, therefore $Y_{l'm'}$ and Y_{lm} must have equal parity, i.e., $V_{l'm',lm}^M(r_i) = 0$ unless $(-1)^{l'} = (-1)^l$.

The first selection rule applies to all linear molecules and the second selection rule applies to all inversion symmetric molecules. Due to the selection rules we may arrange the basis functions in an order that block diagonalizes the matrix representing the molecular potential

$$\mathbf{V}^M(r_i) = \begin{pmatrix} \begin{matrix} m=0 \\ \text{Even} \end{matrix} & & & & & & \mathbf{0} \\ & \begin{matrix} m=0 \\ \text{Odd} \end{matrix} & & & & & \\ & & \begin{matrix} m=1 \\ \text{Even} \end{matrix} & & & & \\ & & & \ddots & & & \\ \mathbf{0} & & & & & \begin{matrix} m=l_{\max} \\ \text{Odd} \end{matrix} & \end{pmatrix}. \quad (3.26)$$

It is sufficient to calculate the nonnegative m blocks, since $V_{l'-m,l-m}^M(r_i) = V_{l'm,lm}^M(r_i)$. When this matrix is exponentiated we just consider the blocks separately. Instead of diagonalizing one matrix of dimension $(l_{\max} + 1)^2$ by $O(l_{\max}^6)$ operations we only need to diagonalize $2(l_{\max} + 1)$ matrices of dimensions between 1 (when l_{\max}) and $l_{\max}/2 + 1$ (when $m = 0$) which requires of the order $O(l_{\max}^{3.5}/4)$ operations. The time saving obtained by exponentiating the block diagonal matrix instead of the full matrix does not lead to an essential overall time saving factor since we only need to exponentiate once anyway. However, after having performed the matrix exponentiation we can be completely sure that the exponentiated matrix will preserve the same block diagonal structure. In each time step the constant exponentiated matrix will be multiplied by the $\mathbf{f}(r_i, t)$ vector. Instead of performing a full matrix multiplication it is only necessary to perform a number of block matrix multiplications within the blocks. This property leads to a significant overall computational saving.

The time dependent field interaction

The field interaction is time dependent and a number of matrix operations, Eqs. (3.12)-(3.17), needs to be performed in every time step. Suppose we orient a z -axis parallel to the the field direction. Of course, we cannot in general take the freedom to align the z -axis parallel to *both* the molecular axis (the molecular frame) *and* the field direction (the lab frame). However, we will show below that we can easily translate the $\mathbf{f}(r_i, t)$ vector from one frame into the other and reverse. Thus, we can represent V^M in the molecular frame with z -axis parallel to the molecular axis and V^F in the lab frame with a z -axis parallel to the field axis as long as we apply them to the $\mathbf{f}(r_i, t)$ vector which refers to the appropriate frame. The possibility of transforming between the two frames is a key concept of the present method since the full three-dimensional propagation of the total potential now effectively reduces to the propagation of two *two*-dimensional propagations.

The field interaction will now be written as

$$V^F(\mathbf{r}, t) = \mathbf{F}(t) \cdot \mathbf{r} = F(t)z = F(t)\sqrt{\frac{4\pi}{3}}rY_{10}(\cos\theta), \quad (3.27)$$

and the corresponding matrix elements are

$$V_{l'm', lm}^F(r_i, t) = F(t)\sqrt{\frac{4\pi}{3}}r_i\langle l'm'|Y_{10}(\cos\theta)|lm\rangle. \quad (3.28)$$

Again, the azimuthal symmetry allows for a block diagonalization in m blocks. Even with this block diagonalization it is very expensive to perform the matrix exponentiation in every time step, Eqs. (3.13) and (3.14). We can avoid the construction of the matrix exponentiation from scratch by noting that the time dependent part of $\mathbf{V}^F(r_i, t)$ is simply a multiplicative factor

$$\mathbf{V}^F(r_i, t) = F(t)\sqrt{\frac{4\pi}{3}}r_i\tilde{\mathbf{V}}. \quad (3.29)$$

The matrix elements of $\tilde{\mathbf{V}}$ are

$$\tilde{V}_{l'm', lm} = \tilde{V}_{l'-m', l-m} = \delta_{m'l'm}\langle l'm|Y_{10}(\cos\theta)|lm\rangle, \quad (3.30)$$

which depend on neither t nor r_i . We may now simplify the matrix exponentiation, Eq. (3.14), according to

$$e^{-i\Delta t\mathbf{V}^F(r_i, t)} = \left(e^{\tilde{\mathbf{V}}}\right)^{-i\Delta tF(t)\sqrt{\frac{4\pi}{3}}r_i} \quad (3.31)$$

$$= \tilde{\mathbf{U}} \cdot e^{-i\Delta tF(t)\sqrt{\frac{4\pi}{3}}r_i\tilde{\mathbf{d}}} \cdot \tilde{\mathbf{U}}^\dagger. \quad (3.32)$$

$\tilde{\mathbf{U}}$ is the *constant* unitary matrix that diagonalizes $\tilde{\mathbf{V}}$ to the diagonal form $\tilde{\mathbf{d}}$. The strategy is now to calculate and store $\tilde{\mathbf{U}}$ and $\tilde{\mathbf{d}}$ once and for all. The construction of

$e^{-i\Delta t \mathbf{V}^F(r_i, t)}$ then reduces to an exponentiation of the diagonal elements, $e^{-i\Delta t F(t) \sqrt{\frac{4\pi}{3}} r_i \tilde{d}_{jj}}$, followed by two matrix multiplications which are block diagonal in m . Having obtained $e^{-i\Delta t \mathbf{V}^F(r_i, t)}$ it should act on $\mathbf{f}(r_i, t)$ which we must ensure is expressed in the lab frame. As our starting point we know $\mathbf{f}(r_i, t)$ in the molecular frame and the elements of $\mathbf{f}(r_i, t)$ are then expansion coefficients to the spherical harmonics referring to the molecular frame. Suppose the lab frame is rotated by the Euler angles ($\alpha = 0, \beta, \gamma = 0$) with respect to the molecular frame. By applying a rotation operator, we obtain the set of expansion coefficients in the rotated frame. In the spherical harmonics basis this transformation is obtained by a matrix multiplication with a unitary rotation matrix \mathbf{D}

$$\mathbf{f}^{(\text{lab})}(r_i, t) = \mathbf{D}(0, \beta, 0) \cdot \mathbf{f}(r_i, t), \quad (3.33)$$

where $\mathbf{f}^{(\text{lab})}(r_i, t)$ is the vector which contains the expansion coefficients to the spherical harmonics referring to the lab fixed frame. The rotation matrix is block diagonal in l so that the elements of $\mathbf{f}^{(\text{lab})}(r_i, t)$ are

$$f_{lm}^{(\text{lab})}(r_i, t) = \sum_{m'=-l}^l \mathcal{D}_{mm'}^{(l)}(0, \beta, 0) f_{lm'}(r_i, t), \quad (3.34)$$

where $\mathcal{D}_{mm'}^{(l)}(0, \beta, 0)$ is a Wigner rotation function. When we have obtained $\mathbf{f}^{(\text{lab})}(r_i, t)$, we multiply by $e^{-i\Delta t \mathbf{V}^F(r_i, t)}$ in order to propagate the field interaction in the lab frame. Finally, we return to the molecular frame $\mathbf{f}(r_i, t)$ by the inverse transformation of Eq. (3.33). In summary, the total propagation of $\mathbf{f}(r_i, t)$ by the field interaction may be written

$$\mathbf{f}(r_i, t + \Delta t) = \mathbf{D}^\dagger(0, \beta, 0) \cdot e^{-i\Delta t \mathbf{V}^F(r_i, t)} \cdot \mathbf{D}(0, \beta, 0) \cdot \mathbf{f}(r_i, t). \quad (3.35)$$

If $\beta = 0$ the lab frame and the molecular frame are identical. The forward and backward rotations may then be omitted and, accordingly, the rotation matrices reduce to the identity matrices.

3.2.2 Benchmark: spherical harmonics- versus space representation

The huge advantage of propagating the potential in the space representation is the great versatility of this method. It hardly matters how complicated the potential may be; one can still use it to propagate without a significantly larger computational cost than what is needed to construct and decompose the wave function (which involves $8l_{\text{max}}^4$ operations). When propagating in the spherical harmonics basis, the computational cost will depend on the symmetry of the potential. In general, it will be equally versatile as the space representation if we simply use the algorithm proposed in Eqs. (3.12)-(3.17). However, this general method is much slower than using space representation. By calculating some matrices only once, it is possible to reduce the calculational cost significantly as we demonstrated in Sec. 3.2.1. In Table 3.1 we have summarized the approximate number of operations required to propagate in the spherical harmonics

	V^M				V^F	
	General	Even	Linear	Linear Even	General	Linear
Initial calculation	l_{\max}^6	$l_{\max}^6/4$	$l_{\max}^{3.5}$	$l_{\max}^{3.5}/4$	l_{\max}^6	$l_{\max}^{3.5}$
Propagation	l_{\max}^4	$l_{\max}^4/2$	$2l_{\max}^{2.5}$	$l_{\max}^{2.5}$	l_{\max}^6	$l_{\max}^{3.5}$

Table 3.1: The number of operations involved in propagation of the potential in spherical harmonics representation depending on the symmetries of the static and time dependent potentials, V^M and V^F respectively. The number of spherical harmonics are restricted by $0 \leq l \leq l_{\max}$ and the total number of basis functions is $(l_{\max} + 1)^2$.

basis. The symmetry dependence arises from the degree of block diagonalization that can be obtained due to selection rules. From Table 3.1 we see that the computational cost is comparable to propagation in the space representation if the time dependent potential is axially symmetric. For H_2^+ we have tested both methods and we have found the propagation in the spherical harmonics basis to be approximately a factor of 40 faster than in the space representation for $l_{\max} = 15$ and, additionally, the numerics of the former method is more stable.

3.2.3 Extension to multielectron molecules

The calculation of the full multi-electron dynamics is impossible with the current computational power and consequently we must again rely on an effective one-electron description. In a single active electron picture we assume that the active electron is only affected by a mean field potential generated by the inactive electrons. If we try to follow the lines of the Hartree-Fock approximation we find that the effective potential seen by the active electron can be divided into three parts. These are a nuclear attraction part, a Coulombic repulsion from the inactive electrons, and a part which arises from the exchange antisymmetry dictated by the Pauli principle. The nuclear attraction is straightforward to implement since the structure of this term is similar to the H_2^+ potential. The Coulomb potential is equal to the classical electrostatic repulsion

$$V_{\text{Coul}}(\mathbf{r}) = \int \frac{\rho(\mathbf{r}')}{|\mathbf{r} - \mathbf{r}'|} d\mathbf{r}', \quad (3.36)$$

where ρ is the electron density which is easily determined by the orbitals from a Hartree-Fock calculation. The exchange potential is on the other hand much more difficult to handle since it is non-diagonal in space representation. One simple approach to obtain a diagonal potential is to use the Slater $X\alpha$ exchange potential

$$V_{\text{XC}}(\mathbf{r}) = -\alpha \left(\frac{3\rho(\mathbf{r})}{8\pi} \right)^{1/3}, \quad (3.37)$$

where α is a parameter that can be adjusted to reproduce the correct binding energy of the electron. We may see this method as a simple density functional method where

the unknown exchange energy functional is approximated by the exchange energy of a uniform electron gas of constant density. With the approximate exchange potential, the total effective potential is in the form $V^M(\mathbf{r})$ and can be inserted into Eq. (3.19). The matrix elements cannot be carried out analytically as in the case of H_2^+ , Eq. (3.25), but can easily be evaluated numerically. When the matrix elements are evaluated, the remaining calculation runs at the same computational cost as in the case of H_2^+ if the molecule is diatomic and homonuclear.

3.3 Ionization probability

In order to simulate the dynamics of the active electron, we need to find an appropriate initial state which should be an eigenstate of the field-free Hamiltonian $H_0 = p^2/2 + V^M(\mathbf{r})$. One method to find the field-free ground state is to propagate in reverse imaginary time. We substitute $t \rightarrow -i\tau$ and integrate the Schrödinger equation

$$\Psi(\mathbf{r}, -i\tau - i\Delta\tau) = \exp(-\Delta\tau H_0)\Psi(\mathbf{r}, -i\tau) \quad (3.38)$$

$$= e^{-\Delta\tau E_0}c_0\psi_0 + e^{-\Delta\tau E_1}c_1\psi_1 + \dots \quad (3.39)$$

In the last line we have expanded Ψ in eigenstates of H_0 , where the eigenstates ψ_n and eigenenergies E_n are unknown at this stage. We see that when we let Ψ evolve in imaginary time the excited components decay faster than the ground state component. We renormalize Ψ in every time step in order to avoid a total decay or explosion of the wave function. If we start out with an arbitrary function as the initial guess for Ψ , we would expect that it would converge towards the ground state ψ_0 . A notable exception is the case where c_0 initially is zero, i.e., when the initial guess is orthogonal to the ground state. In this case, propagation in imaginary time will recover the lowest lying excited state with non-zero projection. An example where this becomes useful is when we want to find the HOMO of O_2 which is the lowest lying π_g orbital. However, several orbitals with lower energy exist but these are all of σ_g , σ_u , and π_u symmetry. In this case we would choose an initial guess on the form $\Psi(\mathbf{r}, 0) = f(r)Y_{21}(\hat{\mathbf{r}})$ since this function is orthogonal to all σ ($m = 0$) and all ungerade (l odd) states.

After the field-free eigenstate is found by propagation in imaginary time, we use it as the initial wave function for the real time propagation. It is inconvenient to use a Gaussian temporal profile for the laser pulse since it has an infinite extension in time. Instead we will use a sine square function to describe the vector potential

$$\mathbf{A}(t) = \frac{\mathbf{F}_0}{\omega} \sin^2\left(\frac{\pi t}{T_{\text{pulse}}}\right) \sin(\omega t), \quad 0 < t < T_{\text{pulse}}, \quad (3.40)$$

which leads to the field $\mathbf{F}(t) = -\partial_t \mathbf{A}(t)$ of finite extension. When we have propagated the wave function through the pulse we wish to know the ionization probability. One method is calculate the survival probability by projecting the wave function on the bound states and then get the ionization probability by probability conservation. This method has the drawback that the Coulombic attraction typically supports infinitely

many bound Rydberg states which have to be found. Another possibility for obtaining the ionization probability is to apply an absorbing boundary at the edge of the radial grid. An absorbing potential can be represented by adding an imaginary potential to the Hamiltonian. This potential should be localized at the outer boundary of the radial grid. Now the time evolution operator becomes non-unitary and the norm is no longer conserved. If we let the wave function evolve some time after the end of the pulse, the continuum part will move towards the boundary of the grid. Here the imaginary potential will ideally remove the whole continuum part of the wave function. After the continuum parts have been removed we calculate the norm of the remaining part which again defines the survival probability. The absorbing imaginary potential should be properly configured and tested. If it is turned on too suddenly, over a few number of radial grid points, it may cause reflection instead of absorption and if it is turned on over a large number of grid points it may absorb parts that belong to the bound states.

4. Outlook

In the nearest future we will continue the work on the split step method. With the current version of the computer code we are immediately able to calculate the ionization probability of a multi-electron molecule along the lines proposed in Sec. 3.2.3. It will be interesting to compare the results of such a calculation on, e.g., N_2 with the equivalent results obtained with the MO-SFA and MO-ADK models.

Differential ionization probabilities such as energy spectra and angular distributions are somewhat more difficult to obtain than the total ionization probability. We cannot yet calculate such quantities but hopefully it will not be too difficult to extend the code for these purposes. For the angular distribution we plan to calculate the quantum mechanical probability current through a solid angle surface at a large distance. We can get the energy spectrum by projections on continuum eigenfunctions of the field-free Hamiltonian. For the centrally symmetric Coulomb potential these continuum wave functions are well studied and energy spectra have already been obtained for atomic hydrogen [34]. In general it is, however, a major difficulty to generate these eigenfunctions. One idea would be to set up a matrix representation of the Hamiltonian in some basis of orthogonal functions and obtain the eigenfunctions by diagonalization. The boundary conditions from the finite radial grid impose a restriction on the allowed energies. In order to obtain results that are independent of radial grid size we would divide the energy scale in some intervals, and in each interval sum the projection of the wave function on all eigenfunctions with an energy within the given interval. This result should be independent of the radial grid.

Next, we plan to include nuclear dynamics. If the nuclei are heavy, a classical description of the nuclear dynamics may be sufficient. In the classical model we will let the nuclei move according to Newton's second law in a potential which is generated by the instantaneous mean field of the electrons. Such a description should be fairly easy to implement. In a quantum mechanical description of the nuclear dynamics, we should add extra terms in the Hamiltonian corresponding to the nuclear kinetic energy and field-nuclei interactions. In a center of mass frame and neglecting rotations we need one extra coordinate to describe the nuclear motion of a diatomic molecule, namely the internuclear distance. In addition to the three electronic coordinates and time we then seek a solution to a five dimensional partial differential equation. To our knowledge, we would be the first to solve this problem if we succeed.

We also plan to use the split step code to calculate the high-order harmonic spectra of molecules. The frequency dependent spectral density is calculated from the Fourier transform of the dipole acceleration. In such a calculation we need a large spatial grid in order to describe the excursion of the continuum electronic wavepacket in the laser field. Additionally, the wavepacket will be confined to propagate mainly along the direction of the laser field. A function which is confined in angles is a superposition of many spherical harmonics and we should remember that the computational cost grows fast with the number of spherical harmonics in the basis. Therefore the spherical grid may not be the most optimal to use for calculation of high-order harmonics.

In a more distant future, it would be interesting to investigate effects of electron-electron correlation. Correlation effects are expected to be important for the proper description of multiple ionization as well as for any dynamics of molecules where the uncorrelated Hartree-Fock description is inadequate. One example of such a highly correlated system is the F_2 molecule. Although several uncorrelated calculations have been made on this molecule [16, 35] none have succeeded to explain the ionization yields observed experimentally. Unfortunately electron-electron correlations are intrinsically difficult to handle and the complexity of the problem increases fast as the number of correlated electrons increases.

Bibliography

- [1] T. K. Kjeldsen, C. Z. Bisgaard, L. B. Madsen, and H. Stapelfeldt, *Phys. Rev. A* **68**, 063407 (2003).
- [2] T. K. Kjeldsen and L. B. Madsen, *J. Phys. B: At. Mol. Opt. Phys.* **37**, 2033 (2004).
- [3] T. K. Kjeldsen, C. Z. Bisgaard, L. B. Madsen, and H. Stapelfeldt, *Phys. Rev. A* **71**, 013418 (2005), e-print: [physics/0409150](#)
- [4] T. K. Kjeldsen and L. B. Madsen, *Phys. Rev. A* **71**, 023411 (2005), e-print: [physics/0411221](#)
- [5] T. K. Kjeldsen and L. B. Madsen (2005), e-print: [physics/0501157](#)
- [6] P. B. Corkum, *Phys. Rev. Lett.* **71**, 1994 (1993).
- [7] L. V. Keldysh, *Sov. Phys. JETP* **20**, 1307 (1965).
- [8] F. H. M. Faisal, *J. Phys. B: At. Mol. Phys.* **6**, L89 (1973).
- [9] H. R. Reiss, *Phys. Rev. A* **22**, 1786 (1980).
- [10] M. V. Ammosov, N. B. Delone, and V. P. Krainov, *Sov. Phys. JETP* **64**, 1191 (1986).
- [11] L. B. Madsen, *Phys. Rev. A* **65**, 053417 (2002).
- [12] G. F. Gribakin and M. Y. Kuchiev, *Phys. Rev. A* **55**, 3760 (1997).
- [13] E. U. Condon, *Phys. Rev.* **36**, 1121 (1930).
- [14] M. W. Schmidt, K. K. Baldrige, J. A. Boatz, S. T. Elbert, M. S. Gordon, J. H. Jensen, S. Koseki, N. Matsunaga, K. A. Nguyen, S. J. Su, et al., *J. Comput. Chem.* **14**, 1347 (1993).
- [15] J. Kobus, L. Laaksonen, and D. Sundholm, *Comput. Phys. Commun.* **98**, 346 (1996).
- [16] X. M. Tong, Z. X. Zhao, and C. D. Lin, *Phys. Rev. A* **66**, 033402 (2002).
- [17] D. M. Brink and G. R. Satchler, *Angular Momentum* (Oxford University Press, London, 1968).
- [18] B. M. Smirnov and M. I. Chibisov, *Sov. Phys. JETP* **22**, 585 (1966).
- [19] A. M. Perelomov, V. S. Popov, and M. V. Terent'ev, *Sov. Phys. JETP* **23**, 924 (1966).
- [20] C. Z. Bisgaard and L. B. Madsen, *Am. J. Phys.* **72**, 249 (2004).

-
- [21] Y. Liang, A. Talebpour, C. Y. Chien, and S. L. Chin, *J. Phys. B: At. Mol. Opt. Phys.* **30**, 1369 (1997).
- [22] I. V. Litvinyuk, K. F. Lee, P. W. Dooley, D. M. Rayner, D. M. Villeneuve, and P. B. Corkum, *Phys. Rev. Lett.* **90**, 233003 (2003).
- [23] A. Talebpour, C. Y. Chien, and S. L. Chin, *J. Phys. B: At. Mol. Opt. Phys.* **29**, L677 (1996).
- [24] A. Talebpour, S. Larochelle, and S. L. Chin, *J. Phys. B: At. Mol. Opt. Phys.* **31**, 2769 (1998).
- [25] C. Guo, M. Li, J. P. Nibarger, and G. N. Gibson, *Phys. Rev. A* **58**, R4271 (1998).
- [26] M. J. Dewitt, E. Wells, and R. R. Jones, *Phys. Rev. Lett.* **87**, 153001 (2001).
- [27] E. Wells, M. J. Dewitt, and R. R. Jones, *Phys. Rev. A* **66**, 013409 (2002).
- [28] X. Urbain, B. Fabre, E. M. Staicu-Casagrande, N. de Ruelle, V. M. Andrianarijaona, J. Jureta, J. H. Posthumus, A. Saenz, E. Baldit, and C. Cornaggia, *Phys. Rev. Lett.* **92**, 163004 (2004).
- [29] B. Fabre, J. H. Posthumus, V. Adrianarijaona, J. Jureta, and X. Urbain, *Laser Phys.* **13**, 964 (2003).
- [30] B. Fabre, J. H. Posthumus, L. Malfaire, E. M. Staicu-Casagrande, J. Jureta, C. C. E. Baldit, and X. Urbain, *Laser Phys.* **14**, 468 (2004).
- [31] M. R. Hermann and J. A. Fleck, *Phys. Rev. A* **38**, 6000 (1988).
- [32] J. P. Hansen, T. Sorevik, and L. B. Madsen, *Phys. Rev. A* **68**, 031401(R) (2003).
- [33] T. Birkeland, Master's thesis, Institutt for Fysikk og Teknologi, Universitetet i Bergen (2004).
- [34] T. Birkeland, M. Førre, J. P. Hansen, and S. Selstø, *J. Phys. B: At. Mol. Opt. Phys.* **37**, 4205 (2004).
- [35] J. Muth-Böhm, A. Becker, and F. H. M. Faisal, *Phys. Rev. Lett.* **85**, 2280 (2000).